Impact of Random Spatial Truncation and Reciprocal-Space Binning on the Detection of Hyperuniformity in Disordered Systems

Yuan Liu ^{1*}, XuRui Li ^{1*}, Jianxiang Tian ^{12†}, Xunwang Yan^{1†} and Ge

Zhang^{3†}

Department of Physics, Qufu Normal University, Qufu, 273165, PR China
 Department of Physics, Dalian University of Technology, Dalian, 116024, PR China
 Department of Physics, City University of Hong Kong, Kowloon, 518057, Hong Kong China

*These authors contributed equally to this work

†Corresponding authors

jxtian@qfnu.edu.cn

xwyan@qfnu.edu.cn

gzhang37@cityu.edu.hk

Abstract: We study how finite-window sampling (random spatial truncation) and reciprocal-space radial binning influence the detection of hyperuniformity in disordered systems. Using thirteen representative two-dimensional simulation systems (two stealthy hyperuniform systems with distinct constraint parameters $\chi=0.20$ and $\chi=0.49$; hyperuniform Gaussian pair statistics system; six hyperuniform targeted S(k) systems with distinct α =0.5, 0.7, 1.0, 1.3, 1.5, 3.0, random sequential addition system; Poisson points distribution system; Lennard-Jones fluid system and Yukawa fluid system) and two real biological systems (avian photoreceptor patterns and looped leaf vein networks), we apply random spatial truncation, re-embed cropped sets at fixed number density, and compute the ensemble-averaged structure factor S(k) and the local number variance $\sigma_N^2(R)$ to detect whether the obtained new finite-sized ensembles preserve the salient structural properties of the original ones. Our numerical protocol addresses limited ensemble sizes (e.g., number of configurations $N_c \le 20$) and small, finite sample regions, which are often encountered in the analysis of experimental imaging data. We find that moderate random spatial truncation (i.e., randomly extracting a smaller subwindow from the original full-field configuration) does not change qualitatively the hyperuniformity classification of the systems. Specifically, disordered hyperuniform systems retain their respective hyperuniformity classes despite a modest reduction in measured hyperuniformity exponent α (i.e., reduction in small-k suppression). Moreover, spatial truncation commonly induces configuration-dependent fluctuations of small-k values of S(k). We show that modest reciprocal-space radial pooling (controlled by a binning parameter m) effectively smooths such spurious

wiggles without changing the hyperuniformity class. Practical guidelines for choosing m, cross-checking spectral fits with the local number variance scaling, and increasing effective sampling are provided. These results provide concrete, low-cost and effective methodology for robust spectral detection of hyperuniformity in finite and truncated datasets which abound in experimental systems.

I. INTRODUCTION

Hyperuniform systems constitute a class of many-body systems with distinctive structural correlations, characterized by the anomalous suppression of density fluctuations in the long-wavelength (large-scale) limit. Unlike ordinary disordered systems such as typical fluids and amorphous solids, hyperuniform systems exhibit qualitatively different large-scale fluctuation behavior. Perfect crystals, perfect quasicrystals, and certain special disordered states all belong to the hyperuniform category [1]. The concept of hyperuniformity provides a unified framework for the classification and structural characterization of crystals, quasicrystals, and those special disordered systems [2-4].

Research on hyperuniformity has recently emerged as an interdisciplinary field and is being actively pursued in diverse directions, including photonic and phononic band-gap materials [5-9], antenna and laser design [10], the thermal properties of stealthy hyperuniform materials [11-12], transport phenomena and critical currents in superconductors [13], diffusion in two-phase media [14-17], properties in condensed matter [18], and various problems in pure mathematics [19-22]. Besides, research on hyperuniformity has extended to the property studies of various systems, such as the investigation into network systems [23], the research on cell motility [24], the studies of classical and quantum spin liquids [25], the self-assembly of robotic spinners with threefold symmetric magnetic binding sites [26], the properties of chromatophores on squid skin [27], the construction of digital realizations [28], the characterization of two-dimensional strictly jammed polydisperse circular-disk packings [29], and the complex dynamic behaviors induced by cross-layer interactions in multilayer systems [30]. These studies have found extensive applications in the design and optimization of novel disordered hyperuniform (DHU) materials [31-37].

As investigations into the relationships between microscopic structure and function in biological systems deepen, the significance of hyperuniformity across biological scales has become increasingly evident and empirically supported. In avian retinae, the photoreceptor cones exhibit a hyperuniform spatial organization. By suppressing long-wavelength density fluctuations, this arrangement enhances photon-capture efficiency and optimizes signal encoding, thereby supporting robust visual perception under complex environmental conditions [38]. In the immune system, the self-organization of immune cells likewise displays hyperuniform features that promote efficient spatial allocation of cell types and facilitate coordinated interactions, improving the precision and efficacy of immune responses [39]. At the ecosystem scale, hyperuniform vegetation patterns observed in arid and semi-arid regions are interpreted as adaptive responses to limited water availability and poor soils. Such patterns reduce

local competition, optimize resource exploitation, and help stabilize material cycling and energy flows, with important consequences for ecosystem resilience and function [40]. Additionally, a global study on drylands found that disordered hyperuniformity shapes vegetation patterns in roughly one-tenth of drylands. These patterns appear visually disordered on small scales while maintaining consistent uniformity across larger scales. This self-organization stems from plant-plant or plant-sediment interactions. It enhances water retention, expands the system's aridity tolerance and connects to diverse dryland systems, though it may impede recovery following disturbances [41]. Moreover, leaf vein networks, which are hierarchical self-organized architectures, exhibit disordered hyperuniformity. Geometric constraints from primary veins and branching patterns prevent the veins from evolving into a perfectly ordered lattice, thus the resulting disordered topology aligns with near-optimal network designs for diffusion and transport [42].

In both simulations and experiments, the most direct detection of hyperuniformity is the structure factor S(k), whose small-wavenumber behavior encodes the system's large-scale spatial correlations. For an infinite, statistically homogeneous configuration with number density ρ , S(k) is related to the total correlation function h(r) (where $h(r) = g_2(r) - 1$, and $g_2(r)$ is the pair correlation function of the system) by:

$$S(\mathbf{k}) = 1 + \rho \tilde{h}(\mathbf{k}) \tag{1}$$

where $\tilde{h}(\mathbf{k})$ denotes the Fourier transform of $h(\mathbf{r})$. For isotropic systems S depends only on the scalar wavenumber $k = |\mathbf{k}|$. A configuration is hyperuniform if the structure factor vanishes in the infinite-wavelength limit,

$$\lim_{k \to 0} S(k) = 0 \tag{2}$$

which implies suppression of density fluctuations at arbitrarily large length scales [3]. For finite samples (e.g., a simulation box of linear size L with N points under periodic boundary conditions, or a finite experimental field of view), one computes the configuration-specific structure factor from the particle positions $\{r_i\}$ as [4]:

$$S(\mathbf{k}) = \frac{1}{N} \left| \sum_{j=1}^{N} e^{i\mathbf{k} \cdot \mathbf{r}_j} \right|^2 \qquad (\mathbf{k} \neq 0)$$
 (3)

and then perform ensemble averaging or angular (radial) averaging as appropriate. Note that the forward-scattering term at k=0 is excluded by construction. In practice the allowed discrete wavenumbers are $k=n \cdot (2\pi/L)$ (with integer vector n), so finite systems cannot probe arbitrarily small k. Therefore, reliable assessment of $\lim_{k\to 0} S(k)$ requires extrapolation from the smallest accessible k values, together with careful control of finite-size and sampling noise.

An equivalent, complementary real-space detection is the local number variance $\sigma_N^2(\mathbf{R}) \equiv \langle N^2(\mathbf{R}) \rangle - \langle N(\mathbf{R}) \rangle^2$, which measures particle-number fluctuations inside an observation window of characteristic linear size R. For a statistically homogeneous configuration the mean number is $\langle N(\mathbf{R}) \rangle = \rho v_1(R)$, where ρ is the number density and $v_1(R)$ is the window volume (area in two dimensions). For spherical (or circular) windows the local number variance can be written exactly as:

$$\sigma_N^2(R) = \rho v_1(R) \left[1 + \rho \int_{\mathbb{R}^d} h(\mathbf{r}) \alpha_2(\mathbf{r}; R) d\mathbf{r} \right]$$
 (4)

where $\alpha_2(\mathbf{r}; R)$ denotes the normalized intersection volume of two identical windows whose centers are separated by |r|. The spectral representation of the local number variance makes the equivalence between the real-space and spectral detection explicit. Using the window indicator $w(\mathbf{x}; R)$ and its Fourier transform $\widetilde{w}(\mathbf{k}; R)$, one may write the local number variance in Fourier space as [3]:

$$\sigma_N^2(\mathbf{R}) = \langle N(R) \rangle \frac{1}{(2\pi)^d} \int_{\mathbb{R}^d} S(\mathbf{k}) \tilde{\alpha}_2(\mathbf{k}; R) d\mathbf{k}$$
 (5)

where $\tilde{\alpha}_2(\mathbf{k}; R)$ is the Fourier transform of the scaled intersection-volume function $\alpha_2(\mathbf{r}; R)$. This identity shows that suppression of spectral weight at small \mathbf{k} necessarily reduces the contribution of long-wavelength modes to $\sigma_N^2(\mathbf{R})$, and conversely that an anomalously slow (sub-volume) growth of $\sigma_N^2(\mathbf{R})$ implies vanishing spectral weight at $k\rightarrow 0$. Hence, $S(\mathbf{k})$ and $\sigma_N^2(\mathbf{R})$ are mathematically equivalent and therefore complementary, mutually reinforcing detections of disordered hyperuniformity [43-46].

More refined distinctions arise when S(k) vanishes as a power law,

$$S(k) \sim k^{\alpha} \quad (k \to 0)$$
 (6)

which corresponds to a far-field tail $h(r) \sim -r^{-(d+\alpha)}$, more refined distinctions emerge. Here α is referred to as the hyperuniformity exponent [1]. In this scenario, the asymptotic scaling of the local number variance $\sigma_N^2(R)$ can be divided into three categories, and hyperuniform systems are also classified into three corresponding classes [3-4, 47], as detailed in Table I.

TABLE I. Classification of hyperuniform systems by the small-k scaling $S(k) \sim k^{\alpha}$ and the corresponding asymptotic growth of the local number variance $\sigma_N^2(R)$ in d dimensions.

Hyperuniformity class	Value of α	Asymptotic scaling of $\sigma_N^2(R)$ vs R
Class I	$\alpha > 1$	$\sigma_N^2(R) \sim R^{d-1}$
Class II	$\alpha = 1$	$\sigma_N^2(R) \sim R^{d-1} \ln(R)$
Class III	$0 < \alpha < 1$	$\sigma_N^2(R) \sim R^{d-\alpha}$

In hyperuniform systems, the local number variance grows more slowly than the window volume \mathbb{R}^d in all cases, which is the defining hallmark of hyperuniformity

and provides a natural way to rank crystals, quasicrystals and special disordered states by the strength of large-scale fluctuation suppression.

From a practical standpoint, reliable identification of disordered hyperuniformity requires a combined spectral—real-space analysis together with careful control of multiple potential bias sources. Finite simulation domains impose a discrete k-grid that limits direct access to the true $k\rightarrow 0$ regime. Consequently, small-k data must be extrapolated with quantified uncertainties. Moreover, spatial truncation and edge effects may bias estimates of S(k) and hyperuniformity exponent α . In many empirical applications one must analyze only a cropped subregion of a larger system (for example, a finite image of a leaf vein networks [42]), and such spatial truncation commonly induces small-k fluctuations or other artefacts that complicate extrapolation of S(k) and estimation of the hyperuniformity exponent α . Currently, this phenomenon can be clearly observed in some real systems [38-40, 42]. Therefore, if not recognized and mitigated, these truncation-induced artefacts may lead to ambiguity or bias in the estimates of the hyperuniformity exponent α .

The objective of the present work is to systematically explore how spatial truncation and related sampling limitations affect the structure factor S(k) and the local number variance $\sigma_N^2(R)$, to identify the origins of small-k fluctuations, and to develop practical mitigation strategies. Concretely, we (i) analyze controlled simulation systems and apply systematic spatial truncation protocols; (ii) compute S(k) and $\sigma_N^2(R)$ using ensemble averaging across independent configurations and analyze the effects of spatial truncation; (iii) compare curves and fitting results and evaluate the effects of spatial truncation on them; (iv) propose recommended practices to mitigate fluctuations and spurious wiggles, yield reliable estimates of the hyperuniformity exponent α and hyperuniform classification, and apply this strategy to real biological systems. We demonstrate these methods on controlled simulation systems and on real biological systems, showing how the recommended procedures mitigate truncationinduced artefacts and improve the reliability of hyperuniformity assessment. Motivated by the limited number of independent configurations typically available in experimental systems, all systems in this study use a modest ensemble size of N_c =20 configurations for ensemble averaging.

The remainder of the paper is organized as follows. In Sec. II, we introduce the controlled simulation systems and real biological systems, and we present the operational protocols for random spatial truncation (the crop ratio parameter c), reembedding, and reciprocal-space radial binning (the radial binning parameter m) used in our analyses. The core results are presented in Sec. III. Sec. III A gives a global overview of spatial truncation effects across thirteen representative two-dimensional controlled simulation systems. The subsequent results are primarily illustrated using

hyperuniform Gaussian pair statistics ensemble as a representative case. Sec. III B examines the effects of the crop ratio c on spectral and real-space detections. Sec. III C studies the influence of reciprocal-space radial binning m, demonstrates how moderate radial pooling mitigates small-k fluctuations, and provides practical guidance for selecting m. Sec. III D applies the same pipeline to real biological systems (avian photoreceptor mosaics and looped leaf vein networks) and shows that modest radial pooling (here m = 2.0) smooths small-k spurious wiggles without changing inferred hyperuniform classification. In Sec. IV, we summarize the key conclusions of the full paper and outline directions for future work.

II. METHODS

To explore how spatial truncation affects the detection of hyperuniformity in disordered system such as the structure factor S(k) and the local number variance $\sigma_N^2(R)$ [1], we analyzed a set of controlled simulation systems together with two classes of real biological systems. These systems were chosen to span a broad range of spatial correlations and practical data conditions, thereby enabling us to test the effects of spatial truncation on spectral and real-space measures under realistic constraints. All systems analyzed here are two-dimensional and our numerical study emphasizes the realistically limited-ensemble regime (the number of configurations $N_c = 20$) so that conclusions apply directly to experimental data sets of comparable size. For consistency across all simulated and real biological systems, every configuration is first normalized to the unit square $[0,1]\times[0,1]$ and then rescaled to a physical periodic box of side L= $\sqrt{N/\rho}$ at a target number density (we adopt $\rho=1.5$ unless otherwise noted, and N is the number of particles in the system). The structure factors S(k), pair correlation functions $g_2(r)$ and local number variances $\sigma_N^2(R)$ are computed in the periodic box after rescaling. Representative configurations of the thirteen controlled simulation systems are shown in Figure 1 and real biological systems are described in Refs. [38, 42].

A. Controlled simulation systems

We employed thirteen typical two-dimensional point-pattern models as controlled testbeds.

(1) Stealthy hyperuniform system. Stealthy systems are disordered hyperuniform ground states produced by constraining collective density modes (S(k) = 0) for $|\mathbf{k}|$ below a prescribed cutoff. They provide a tunable family of disordered hyperuniform patterns that interpolate between crystals and disordered states as the constraint parameter χ is varied. These ground

- states are generated by collective-coordinate and energy-minimization protocols and exhibit strong suppression of small-k spectral weight and associated anomalous transport and optical properties [48-50]. We included two representative stealthy parameter sets ($\chi = 0.20$ and $\chi = 0.49$) to sample weakly and strongly constrained hyperuniform states.
- (2) Hyperuniform Gaussian pair statistics system. Gaussian pair statistics form a class of target pair correlations whose direct-space and reciprocal-space forms are both Gaussian. The prescribed pair correlation function $g_2(r)$ is Gaussian-like and its Fourier transform is likewise Gaussian, which yields a structure factor that vanishes at the origin with the power-law $S(k) \sim k^2$, corresponding to Class I hyperuniformity. These target statistics are physically realizable, suitable effective pair potentials can be constructed that produce equilibrium ensembles whose $g_2(r)$ and S(k) closely match the Gaussian targets. Because they provide a concrete, realizable example of the disordered hyperuniformity with hyperuniformity exponent $\alpha = 2$, Gaussian pair statistics serve as a convenient canonical reference for benchmarking how finite sampling, spatial truncation, and reciprocal-space binning affect the detection and quantification of hyperuniform order [51].
- (3) Hyperuniform targeted S(k) systems. Systems satisfying the relationship $S(k) \sim k^{\alpha}$ were generated using the algorithm detailed in Ref. [52]. Specifically, the algorithm constructs 100 configurations simultaneously by minimizing the difference between their average structure factor and the target, $S_0(k) = (k/k_{\text{max}})^{\alpha}$, for all $|\vec{k}| < k_{\text{max}}$. Here we chose $k_{\text{max}} = 5$ so that the target is realizable at unit density for every α we explore. We selected six values of α : 0.5, 0.7, 1.0, 1.3, 1.5, and 3.0, which fully cover the three hyperuniformity classes, in order to systematically study sampling limitations in different classes.
- (4) Random Sequential Addition (RSA) system. RSA packings are generated by irreversible, non-overlapping insertions and approach a saturation density with characteristic short-range exclusion and long-range correlations. Near saturation RSA exhibits suppressed local clustering relative to a completely random process but is not generically hyperuniform. RSA systems serve as a nonequilibrium reference with strong local order [53-54]. For this study, we employed near saturation RSA configurations that met two specific criteria: one being 10,000 consecutive failed attempts to insert new particles, the other being an exact particle count of 10,000.
- (5) Poisson points distribution system. The homogeneous Poisson point distribution system serves as the null model for complete spatial disorder. In

- the infinite-size limit it has $S(k) \equiv 1$ and the local number variance scaling $\sigma_N^2(R) \sim R^d$, i.e., no large-scale suppression. It is included as the non-hyperuniform control [55].
- (6) Lennard-Jones (LJ) fluid system. The LJ model is the canonical simpleliquid potential. Depending on state point it can show mild small-k suppression related to compressibility and interparticle correlations but does not generally produce hyperuniform behavior. LJ fluids therefore provide an equilibrium liquid benchmark with realistic short-range structure and thermal noise [56-57]. We employed reduced density $\rho^* = \rho_0 \sigma^3 = 0.8$ and reduced temperature $\beta^* = 1/T^* = \epsilon/(K_b T) = 1.35$, where σ represents the minimum distance between two particles when the LJ potential is exactly zero, ϵ is the depth of the LJ potential well, K_b stands for the Boltzmann constant, ρ_0 represents the density, and T denotes the temperature [56]. We generated configurations of the LJ fluid system via molecular dynamics (MD) simulations, solving the Newtonian equations of motion using the Verlet algorithm [58] until the system properties no longer changed with time. The initial configuration was set to a square lattice, and configurations were periodically sampled every 10,000 time steps. The reduced time step was set to $\Delta t^* = 0.001$ (where the reduced time is defined as $t^* = t\sqrt{\epsilon/m/\sigma}$), and the maximum reduced time was $t_{max}^* = 500$. All configurations were based on the converged results after 5×10^5 time steps, ensuring the system reached full equilibrium.
- (7) One-component Yukawa fluid system. Yukawa (screened-Coulomb) systems model charged colloids and dusty plasmas. By tuning screening and coupling parameters they exhibit a wide range of compressibility and correlation strengths. Under strong coupling and weak screening these systems can display substantial small-k suppression. Nevertheless, they are not generically DHU and therefore serve as a model for long-range repulsive correlations [59-60]. We also employed reduced density $\rho^* = 0.8$ and reduced temperature $\beta^* = 1.35$ consistent with the LJ fluid system. Configurations of the one-component Yukawa fluid were generated using the same MD simulation protocol as detailed for the LJ fluid. The initial configuration was likewise set to a square lattice, and configurations were periodically sampled every 10,000 time steps during the simulation. In addition, this protocol includes the Verlet algorithm [58] for solving Newtonian equations of motion, the reduced time step ($\Delta t^* = 0.001$), the maximum reduced time ($t_{max}^* = 500$), and the convergence criterion (5×10⁵) time steps), all to ensure consistency across the two fluid models.

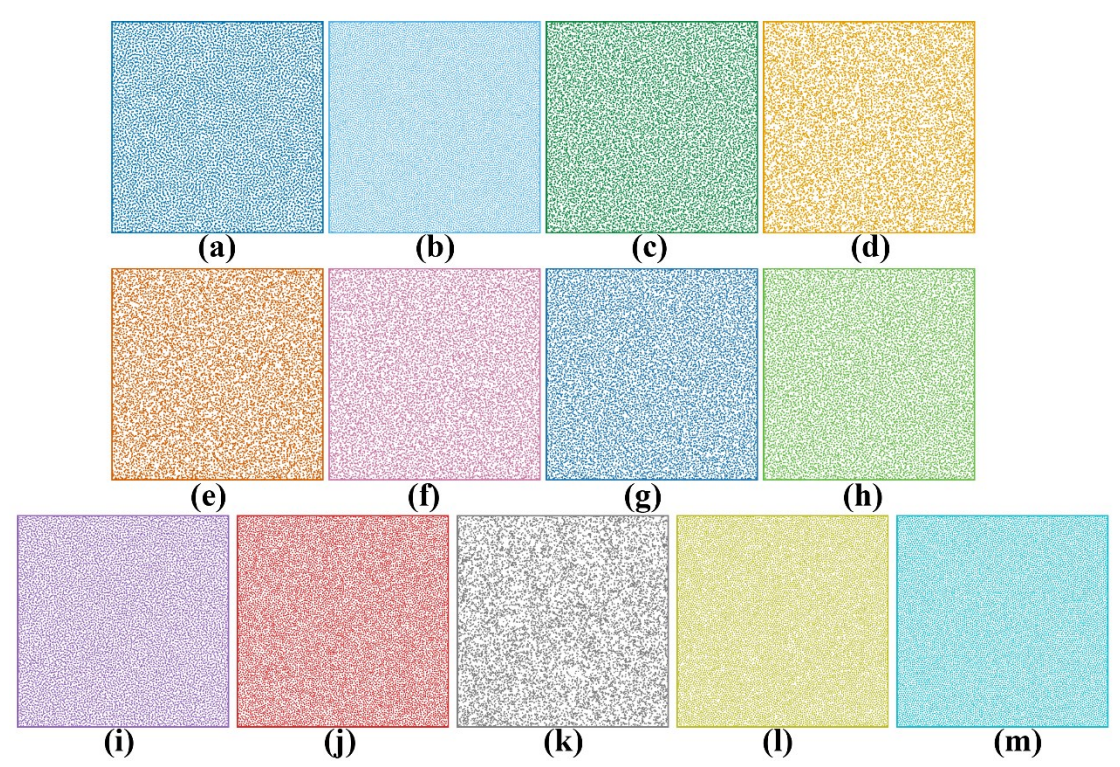


FIG. 1. Representative configurations of the controlled simulation systems used in this study. Each panel shows a single configuration of $N=10^4$ points. Panels: (a-b) stealthy hyperuniform systems with $\chi=0.20$ and $\chi=0.49$, respectively; (c) hyperuniform Gaussian pair statistics system; (d-i) hyperuniform targeted S(k) systems with targeted $\alpha=0.5, 0.7, 1.0, 1.3, 1.5$ and 3.0 respectively; (j) random sequential addition (RSA) system; (k) Poisson points distribution system; (l) Lennard–Jones fluid system; (m) one-component Yukawa fluid system.

B. Real biological systems

To demonstrate practical implications we analyze two classes of real biological systems.

- (1) Avian photoreceptor patterns (bird retina cones). Multitype photoreceptor arrangements in bird retinas were shown to be disordered hyperuniform. Both the combined cone population and many individual cone subtypes exhibit vanishing S(k) as $k\rightarrow 0$, a striking example of biological DHU with functional implications for optimal light sampling. We use published coordinate data sets for chicken retinae as a biologically motivated empirical test case [38].
- (2) Looped leaf vein networks. Recent analyses of looped secondary vein networks demonstrate a universal hyperuniform organization of the cellular loop centers (a biological network tessellation), with measured small-k scaling consistent with disordered hyperuniformity. Leaf vein thus provides another structurally distinct real-world example in which truncated observations and finite sampling are genuine practical issues [42].

C. Cropping ratio parameter and radial binning parameter definitions

To investigate how spatial truncation and finite sampling affect the structure factor S(k) and the local number variance $\sigma_N^2(R)$, we introduce two parameters. All spatial truncation is performed by random square crops. Starting from a configuration in a square box of side L at target number density ρ (so that $L = \sqrt{N/\rho}$, where N is the number of particles in the configuration), we choose a square crop of linear size cL with $0 < c \le 1$. The crop center is chosen uniformly at random. All points whose positions fall inside the crop are kept, yielding a cropped point set with a particle count of N_{crop} . To preserve the target number density ρ for subsequent analysis, the cropped configuration is re-embedded into a periodic square box of side $L_{crop} = \sqrt{N_{crop}/\rho}$, after an affine rescaling of the cropped coordinates from the physical crop side cL to L_{crop} . Thus, c = 1.0 corresponds to no cropping and $L_{crop} = L$; for c < 1, the new side length is not fixed to cL but is recomputed from N_{crop} to enforce the same density ρ . The smallest accessible wave number for the cropped-and-reembedded system is then $k_{min} = 2\pi/L_{crop}$.

Typically, in a periodic box of side L, when calculating the structure factor S(k), the wave number bin width k_{Bin} is $2\pi/L$, i.e., $k = n \cdot (2\pi/L)$ (with integer vector n), so that the natural radial bin width is $2\pi/L$ [1]. To control radial smoothing of the measured structure factor, we introduce a reciprocal-space radial binning parameter m and partition the radial k-axis into uniform bins of width $k_{Bin} = m \cdot (2\pi/L)$. Thus m governs the number of discrete reciprocal vectors pooled into each radial shell. For instance, m = 1.0 corresponds to the fundamental spacing, and larger integer m yields increased radial averaging (stronger smoothing) of the ensemble-averaged structure factor S(k). Notably, wavevector quantization under periodic boundary conditions and finite-size limitations make $m \ge 1.0$ necessary [61-62]. In practice, m is treated as a numerical regularization parameter whose influence is examined as part of the analysis.

For each configuration i in an ensemble of N_c independent configurations we compute the configuration-specific structure factor $S^{(i)}(k)$ on the discrete reciprocal grid, perform radial binning with width k_{Bin} , and obtain the ensemble-averaged structure factor S(k) by averaging across configurations. The local number variance $\sigma_N^{2(i)}(R)$ for each configuration is estimated by sampling many circular observation windows in the periodic re-embedded box and counting the number of particles within each window. Ensemble-averaged local number variance curves are formed by averaging these configuration-specific estimates [1]. We extract the small-k hyperuniformity exponent α from fits to the small-k portion of the ensemble-averaged structure factor S(k). The real-space exponent β is obtained independently from the asymptotic scaling of the ensemble-averaged $\sigma_N^2(R)$. And we use β to cross-check the

III. RESULTS

A. Spatial truncation effects across controlled simulation systems

To evaluate the generic consequences of spatial truncation, we compare spectral and real-space detection across thirteen representative two-dimensional controlled simulation systems. For each model we generated configurations with N=10,000 particles at the target number density ρ , applied random spatial truncation (i.e., randomly extracting a smaller subwindow from the original full-field configuration, and this process is illustrated in Figure 2) with ratio c=0.1, re-embedded the cropped points at the same ρ (see Sec. II C), and then computed the structure factor S(k), the local number variance $\sigma_N^2(R)$ and the pair correlation function $g_2(r)$ for comparison between uncropped and cropped data. All results reported in this section are ensemble averages over $N_c=20$ independent configurations. Figure 2 presents paired comparisons of these detections for all thirteen model classes and Table II summarizes the realized mean cropped particle number \overline{N}_{crop} , fitted hyperuniformity exponent α , the difference in the fitted hyperuniformity exponent α before and after cropping $\Delta \alpha$, and fitted local number variance $\sigma_N^2(R)$ exponent β for the uncropped and cropped systems.

Before discussing the research results, it is important to note that the theoretical value of the hyperuniformity exponent α for each disordered hyperuniform system stems from extensive ensemble averaging, and the α of a single configuration does not strictly match the theoretical value. The number of configurations investigated in this work is limited (N_c =20), which leads to certain deviations between the actually fitted α and the theoretical value. In addition, discrete-k resolution, the choice of radial binning, and errors associated with numerical simulation and fitting processes also induce moderate deviations. Furthermore, Class II hyperuniform systems are defined with α strictly equal to 1.0, but due to the aforementioned errors, it is challenging to obtain an α strictly equal to 1.0 in practical experiments and simulations. Therefore, in this work, we broadly classify hyperuniform systems with α in the range of 0.95 to 1.05 as Class II hyperuniform systems.

TABLE II. Summary of spatial truncation effects. For each model the table lists the crop ratio c, the realized mean cropped particle number \overline{N}_{crop} , the fitted hyperuniformity exponent α obtained from a small-k fit to S(k), the difference in the fitted hyperuniformity exponent α before and after cropping $(\Delta\alpha)$, and the fitted real-space exponent β obtained from the asymptotic scaling of $\sigma_N^2 \sim R^\beta$. All values are reported for uncropped (c=1.0) and cropped (c=0.1) systems.

System	с	\overline{N}_{crop}	α	$\Delta \alpha$	β
G. 14. (0.00)	1.0	10,000	∞		1.01
Stealthy ($\chi = 0.20$) system	0.1	100.2	1.92	∞	1.00
G. 14. (0.40)	1.0	10,000	∞		1.02
Stealthy ($\chi = 0.49$) system	0.1	99.6	1.96	∞	1.02
Hyperuniform Gaussian pair statistics	1.0	10,000	2.04	0.45	0.99
system	0.1	100.5	1.59	0.45	1.00
Hyperuniform targeted $S(k)$ systems	1.0	10,000	0.53	0.04	1.46
(targeted α =0.50)	0.1	98.1	0.49	0.04	1.45
Hyperuniform targeted $S(k)$ systems	1.0	10,000	0.73	0.05	1.25
(targeted α =0.70)	0.1	101.2	0.68	0.05	1.24
Hyperuniform targeted $S(k)$ systems	1.0	10,000	1.02	0.06	1.07
(targeted α =1.00)	0.1	98.9	0.96	0.06	1.05
Hyperuniform targeted $S(k)$ systems	1.0	10,000	1.31	0.16	1.03
(targeted α =1.30)	0.1	100.7	1.15	0.16	1.04
Hyperuniform targeted $S(k)$ systems	1.0	10,000	1.52	0.25	1.00
(targeted α =1.50)	0.1	100.3	1.27	0.25	1.02
Hyperuniform targeted $S(k)$ systems	1.0	10,000	2.97	1.22	0.99
(targeted α =3.00)	0.1	99.7	1.64	1.33	0.98
Random sequential addition (RSA)	1.0	10,000	\	\	1.60
system	0.1	98.7	\	\	1.55
Delice and interdistribution of	1.0	10,000	\	\	1.98
Poisson points distribution system	0.1	94.1	\		1.93
Laurent Laure C. 1	1.0	10,000	\	\	1.51
Lennard-Jones fluid system	0.1	100.4	\	\	1.56
Yukawa fluid system	1.0	10,000	\		1.59
Tunawa Hula System	0.1	101.1	\	\	1.61

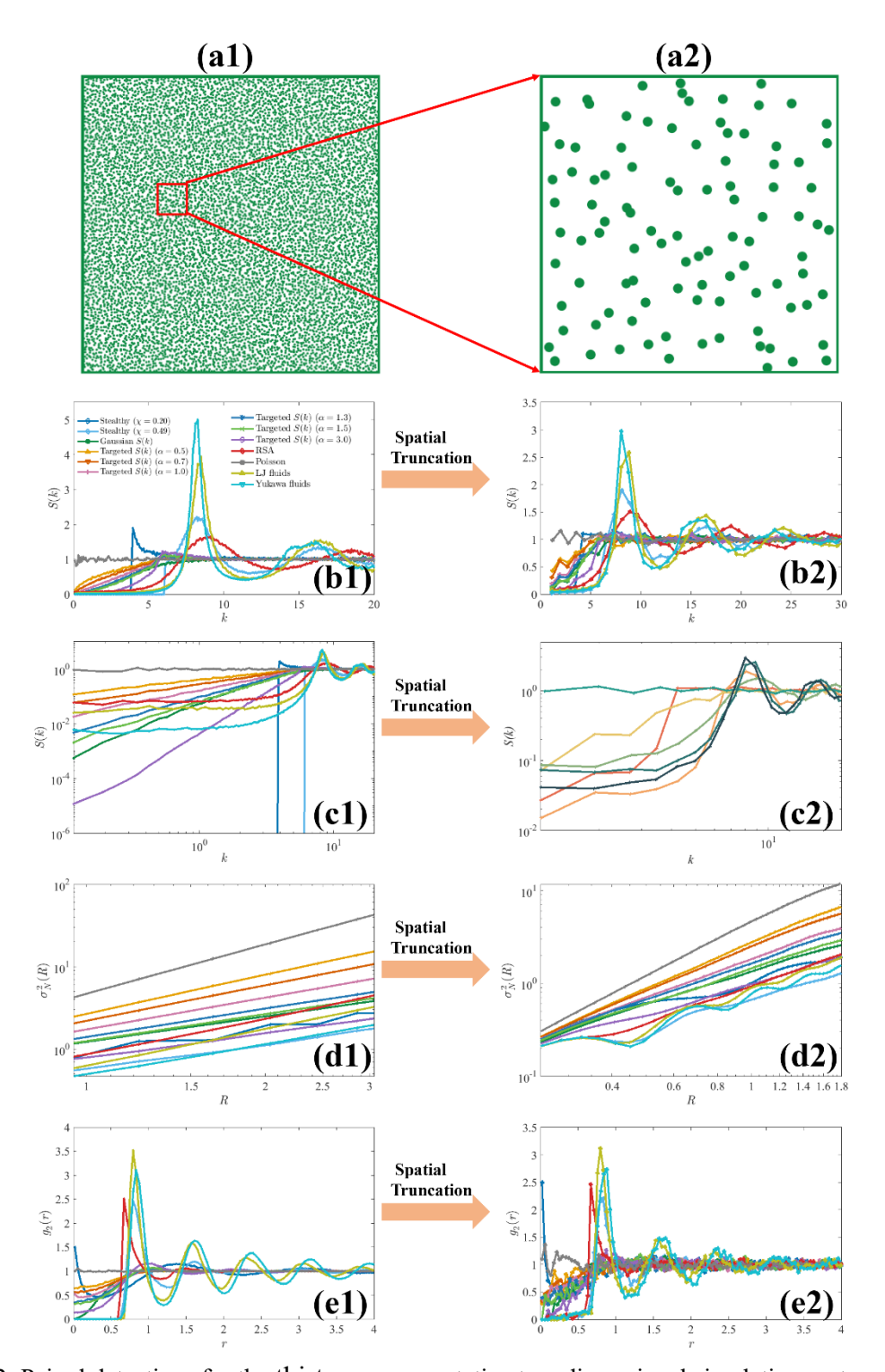


FIG.2. Paired detections for the thirteen representative two-dimensional simulation systems. Left column (a1-e1) shows results for uncropped systems; right column (a2-e2) shows results for systems after random spatial truncation with c=0.1 and re-embedding at the original number density. Panels (a1) and (a2) present the process of random spatial truncation: (a1) shows the full-field configuration with N=10,000 and the red inset indicating the cropping window, and (a2) shows the corresponding cropped configuration with N=100. Panels (b1) and (b2) show the structure factor S(k) on a linear scale. Panels (c1) and (c2) show the same S(k) data on a log-log scale. Panels (d1) and (d2) present the local number variance $\sigma_N^2(R)$ on a log-log scale. Panels (e1) and (e2) display the pair correlation function $g_2(r)$.

For hyperuniform systems (stealthy hyperuniform systems [48-50], hyperuniform Gaussian pair statistics system [51] and hyperuniform targeted S(k) systems [52]), we find that the characteristic small-k suppression of S(k) is retained following cropping, but cropping produces two reproducible effects. First, the hyperuniformity exponent α fitted from ensemble-averaged cropped configurations is systematically reduced compared with the uncropped case, which indicates a modest weakening of longwavelength suppression. Furthermore, it can be observed from Table II that for systems with a larger hyperuniformity exponent α prior to cropping, the magnitude of the reduction in α after cropping is correspondingly greater. Although this reduction is significant for $\alpha = 3$, it diminishes and becomes negligible for $\alpha \le 1$, and therefore does not alter the asymptotic hyperuniform class assignment of the system. Second, cropping at c = 0.1 tends to amplify spectral fluctuations in the very smallest k-bins, inducing nonmonotonic features (wiggles) that may bias small-k fits. Apart from these, short-range structure is robust to spatial truncation, and the overall shapes of $g_2(r)$ and S(k) are preserved. This feature is present across both hyperuniform and nonhyperuniform systems.

For non-hyperuniform systems, Poisson points distribution ensembles remain essentially flat $(S(k) \approx 1)$ before and after cropping, up to sampling noise. Moreover, random sequential addition (RSA) near saturation, the Lennard–Jones (LJ) fluids, and the Yukawa fluids at the chosen liquid state points all exhibit nonzero small-k intercepts in the uncropped state and retain those intercepts after cropping. In particular, spatial truncation does not drive these ensembles toward vanishing $S(k \to 0)$. Short-range structural signatures, including peak positions and multiplicities in $g_2(r)$ and the corresponding peaks in S(k), are robust to cropping across all examined model classes.

The results of local number variance $\sigma_N^2(R)$ corroborate the structure factor S(k) findings. Cropped systems preserve the characteristic scaling of $\sigma_N^2(R)$, class I hyperuniform systems maintain β values close to 1.0, while non-hyperuniform systems retain their original β behavior within sampling uncertainty. Taken together, the spectral and real-space results emphasize that reliable hyperuniformity classification requires joint consideration of both S(k) and $\sigma_N^2(R)$. The findings indicate that while spatial truncation leads to a small reduction in the fitted α , it does not change the system's qualitative properties nor its classification as disordered hyperuniform.

Taken together, these system-level results support three conservative conclusions. First, random spatial truncation at the moderate level studied does not convert non-hyperuniform systems into hyperuniform ones, ensembles that exhibit a finite intercept in S(k) before truncation continue to do so after truncation. Second, for systems that are disordered hyperuniform (i.e., that exhibit strong small-k suppression prior to truncation), spatial truncation weakens the degree of suppression (manifesting as a

reduction in fitted α) but does not change the asymptotic hyperuniformity class as determined by the scaling of S(k) and $\sigma_N^2(R)$. Third, spatial truncation largely preserves short-range structural information (peak positions, peak multiplicities and features in $g_2(r)$ and S(k)). Nevertheless, spatial truncation can induce configuration-dependent fluctuations in the first few small-k bins of S(k). Mechanistically, these effects are attributable to the combined loss of true long-wavelength modes and to discrete-grid and rebinning artifacts that arise when N_{crop} and L_{crop} differ from the uncropped values. Finite-sample noise and configuration dependence further modulate observed small-k behavior, which motivates the ensemble-averaging approach and the subsequent focused analyses of c- and m-dependence in Sec. III B and Sec. III C.

B. Cropping ratio (c) dependence

All results in this subsection are ensemble averages over $N_c=20$ independent configurations. We examine the dependence of spectral and real-space detection on the crop ratio using the hyperuniform Gaussian pair statistics [51] as a representative disordered hyperuniform ensemble. Configurations with N=10,000 particles were cropped with $c \in \{0.1, 0.2, 0.3, 0.4, 0.5, 0.6, 0.7, 0.8, 0.9, 1.0\}$, and each cropped configuration was re-embedded at the target number density ρ as described in Sec. II C. For each c we compute the ensemble-averaged structure factor S(k), the ensemble-averaged local number variance $\sigma_N^2(R)$, and the ensemble-averaged pair correlation function $g_2(r)$. Small-k hyperuniformity exponents α are obtained by fitting the ensemble-averaged S(k) over the small-k portion. The real-space exponent β is obtained by fitting the asymptotic regime of $\sigma_N^2(R)$.

For the hyperuniform Gaussian pair statistics systems, Figure 3 presents S(k), $\sigma_N^2(R)$ and $g_2(r)$ across the cropping-scan, and Table III reports the fitted small-k hyperuniformity exponents α and real-space exponents β for each crop ratio c. The uncropped ensemble (c=1.0) recovers the theoretical small-k scaling $(\alpha \approx 2.04)$, whereas all cropped ensembles $(c \le 0.9)$ exhibit substantially reduced α values clustered in the range $\alpha \approx 1.56 \sim 1.65$. By contrast, the real-space exponent β remains close to unity for the entire c-range (Table III), indicating that the Class I surface-area scaling of $\sigma_N^2(R)$ is preserved even when the fitted spectral slope is diminished. For $0.1 \le c \le 1.0$ all examined configurations remain Class I disordered hyperuniform in the sense of their combined spectral and real-space detection.

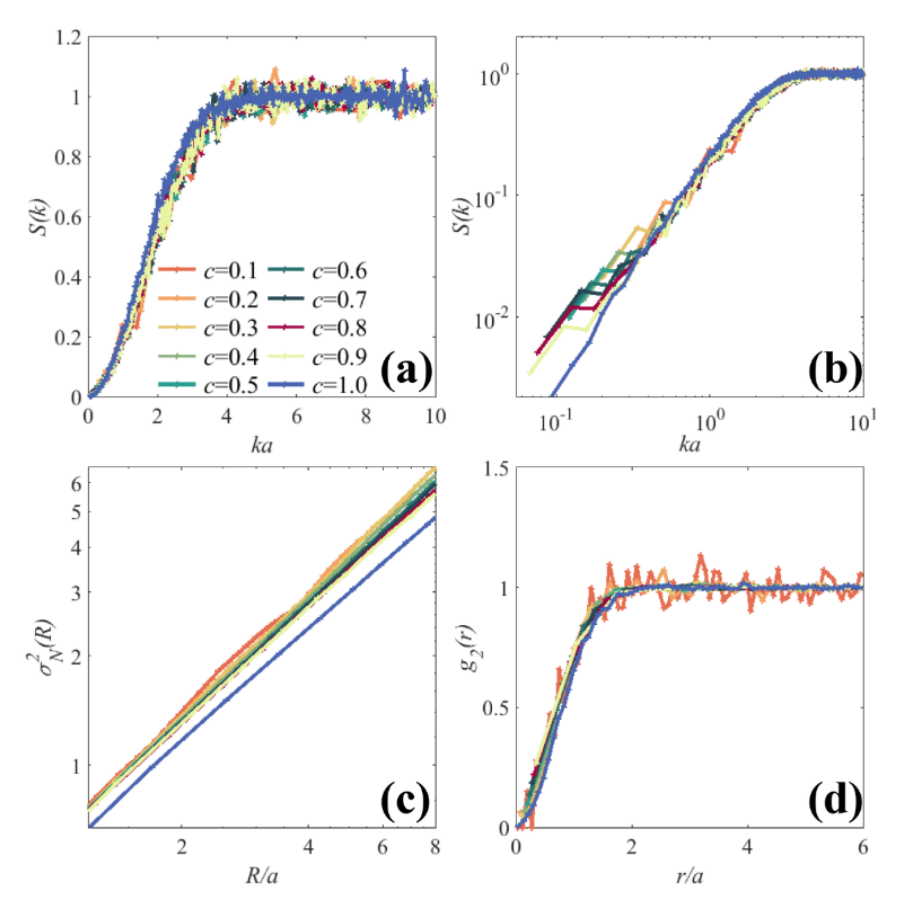


FIG.3. Spectral and real-space detection for the hyperuniform Gaussian pair statistic ensemble under the cropping scan. Here a denotes the ensemble-average nearest-neighbor distance. Panel (a) shows the structure factor S(k) on a linear scale. Panel (b) shows the same S(k) data on a log-log scale. Panel (c) presents the local number variance $\sigma_N^2(R)$ on a log-log scale. Panel (d) displays the pair correlation function $g_2(r)$.

TABLE III. Summary of cropping-scan results for the hyperuniform Gaussian pair statistics systems. For each crop ratio c, the table reports the ensemble-averaged cropped particle number N_{crop} , the fitted hyperuniformity exponent α and the fitted real-space exponent β .

С	\overline{N}_{crop}	α	β
0.1	100.5	1.59	1.00
0.2	400.1	1.56	0.97
0.3	897.7	1.58	1.01
0.4	1601.1	1.60	1.00
0.5	2501.0	1.61	1.03
0.6	3595.2	1.62	1.04
0.7	4896.8	1.57	1.02
0.8	6394.2	1.62	1.03
0.9	8098.4	1.65	1.02
1.0	10000	2.04	0.99

These observations support two key conclusions. First, applying random spatial truncation with re-embedding causes a shift in the measured spectral exponent, moving from the full box to any cropped window lowers the fitted α . Further reductions of c within the cropped regime do not produce a simple monotonic decline because the cropped α values remain clustered in a relatively narrow range. Second, the real-space exponent β stays of order unity for all c, so the asymptotic hyperuniform class inferred from the local number variance scaling, namely Class I, is preserved. The primary mechanism behind these effects is the loss of true long-wavelength modes after spatial truncation, compounded by changes in the discrete-k grid and by radial-rebinning artifacts. Together these reduce the resolvable small-k slope and increase configuration-dependent variability and fluctuations. Finally, to recover theoretical spectral exponents from finite, truncated data we recommend increasing effective sampling through larger N_c , applying stronger radial pooling where appropriate, and cross-checking spectral fits against the local number variance scaling.

Besides, the spatial truncation systematically induces fluctuations in the small-k bins, and its magnitude does not grow monotonically as c decreases. Instead, cropped ensembles at different c show similar degrees of small-k wiggliness. Two mechanisms explain this behavior. First, spatial truncation removes true long-wavelength modes, which increases the relative contribution of intermediate-wavelength fluctuations to the lowest measured bins. Second, the re-embedding step changes the discrete k-grid so that radial rebinning can place bin centers at nodes or antinodes of configuration-specific spectral variations. By contrast, short-range structure is robust to spatial truncation, across the range of c studied the overall shapes of $g_2(r)$ and S(k) are preserved.

In summary, within a reasonable range of crop ratios the overall structural character of the configurations is retained, but spatial truncation commonly induces fluctuations in the small-k bins. The magnitude of this effect shows little systematic dependence on c. Spatial truncation tends to reduce the apparent degree of disordered hyperuniformity as measured by the fitted spectral slope, but this reduction is not strongly sensitive to the exact choice of c and does not change the asymptotic hyperuniform class.

C. Radial binning (m) and mitigation of small-k fluctuations

To address the small-k fluctuations induced by spatial truncation, we study radial smoothing in reciprocal space using the hyperuniform Gaussian pair statistics ensemble [51] at c=0.5 as a representative case. To study the effect of radial smoothing in reciprocal space, we vary the radial binning parameter m. The radial bin width is

 $k_{Bin} = m \cdot 2\pi/L$ with L the side length of the periodic box. Notably, wavevector quantization under periodic boundary conditions and finite-size limitations make $m \ge 1.0$ necessary [61-62]. We examine $m \in \{1.0, 1.2, 1.5, 2.0, 2.5, 3.0, 3.5, 4.0\}$. For each m we form the ensemble-averaged structure factor S(k) and extract the small-k hyperuniformity exponent α . The real-space exponent (the local number variance $\sigma_N^2(R)$ exponent) β is obtained from the asymptotic scaling of the ensemble-averaged number variance $\sigma_N^2(R)$. Figure 4 displays the S(k) curves for the tested m values, Table IV reports the observed minimum plotted wave number k_{\min} and fitted α .

From the numerical results we draw several practical observations. First, moderate increases of m produce visibly smoother S(k) while leaving the overall spectral morphology unchanged. This smoothing reduces the prominence of configuration-dependent fluctuations and improves the stability of visual inspection. Second, the minimum plotted wave number k_{min} does not vary monotonically with m. This effect results from discrete radial binning. When m equals 1.0, the first radial bin may contain no k vectors for a given configuration and the plotted k_{min} then appears in the second bin. Slightly increasing m can place at least one k vector into the first bin and thereby produce a smaller observed k_{min} . This behavior shows that the selected m can influence which small k points are available for plotting and for fitting. Third, very large values of m increase k_{min} substantially and reduce the number of sampled points in the small k region. This data loss can remove information that is critical for determining the small k slope and may bias the fitted α .

Taken together, the optimal choice of m depends on the system, on the specific configurations, and on the severity of fluctuations. It requires a trade-off between visual smoothness and retention of small-k information. Based on the tests reported here, we recommend moderate radial coarse-graining and suggest $1.0 \le m \le 3.0$ as a practical starting range. Determine the smallest m that effectively suppresses spurious wiggles while keeping k_{min} as small as possible by performing an m-scan. When recovering theoretical spectral exponents from finite, truncated data, validate spectral fits using the local number variance scaling. Where feasible, increase effective sampling by averaging over more configurations.

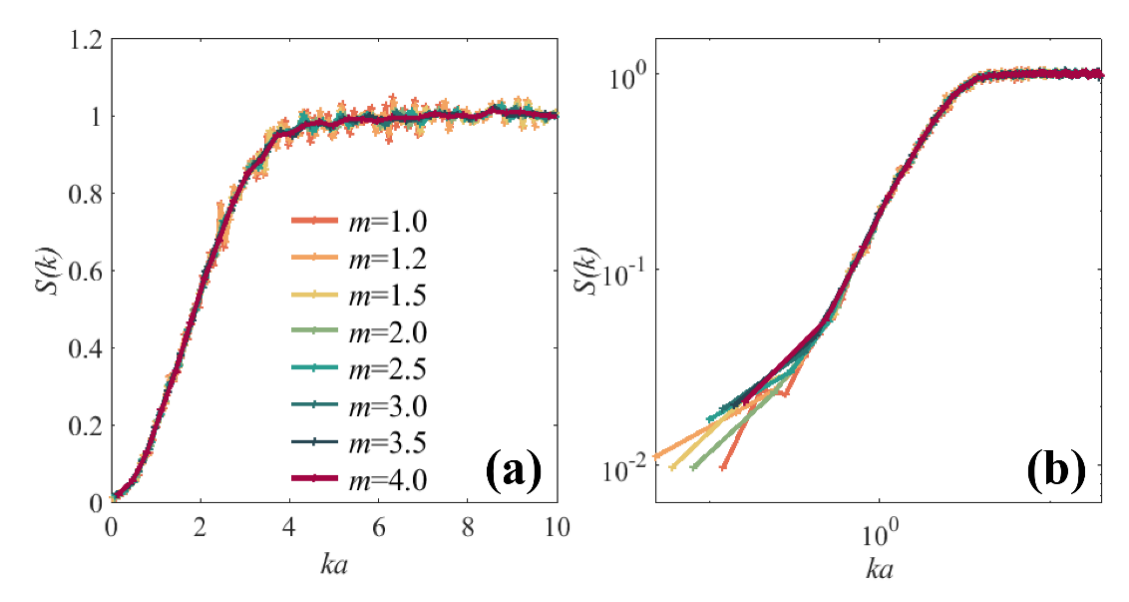


FIG.4. Structure factor S(k) for the hyperuniform Gaussian pair-statistic ensemble (the crop ratio c=0.5) plotted for different radial binning parameters m. Here a denotes the ensemble-average nearest-neighbor distance. Panel (a) shows S(k) on a linear scale. Panel (b) shows the same data on a log-log scale to emphasize small-k behavior.

TABLE IV. Dependence of fitted exponents on the radial-binning parameter m for the hyperuniform Gaussian pair-statistic ensemble at c=0.5. Columns give the radial binning parameter m, the observed minimum plotted wave number (where a is the ensemble-average nearest-neighbor distance), the fitted small-k hyperuniformity exponent α obtained from the ensemble-averaged S(k), and the real-space exponent β obtained from $\sigma_N^2(R)$.

β	α	ka _{min}	m
	1.61	0.120775	1.0
	1.58	0.048310	1.2
	1.56	0.060387	1.5
1.02	1.63	0.080516	2.0
1.03	1.52	0.100646	2.5
	1.50	0.120775	3.0
	1.45	0.140904	3.5
	1.43	0.161033	4.0

D. Application to real biological systems

To test whether the spatial truncation and the reciprocal-space radial binning phenomena observed in controlled simulation systems appear in real biological systems, we applied the same analysis pipeline to two real biological systems previously reported to exhibit disordered hyperuniform organization: avian photoreceptor patterns [38] and looped leaf vein networks [42]. Structure factors S(k) were computed following the

procedures of Sec. II. For the photoreceptor data we selected random square spatial truncation with class-specific crop ratios so that the resulting cropped particle counts N_{crop} are comparable across receptor classes (Red, Green, Blue, Violet, Double, and the combined Overall population). The cropped configurations were re-embedded at fixed number density as described in Sec. II C. For the leaf vein networks, because the configurations were originally obtained by cropping regions from whole leaves and already exhibit pronounced fluctuations, we analyzed the available full fields of view without further cropping.

Figures 5(a)-(b) and 6(a)-(b) show the ensemble-averaged structure factors S(k) on linear and log scales for the cropped avian photoreceptor patterns and for the looped leaf vein networks, respectively. As in the controlled simulation systems, the cropped configurations exhibit varying degrees of small-k fluctuations. Guided by the discussion in Sec. III C, we recomputed S(k) using a reciprocal-space radial binning parameter m=2.0. The corresponding spectra are shown in Figure 5(c)-(d) and 6(c)-(d). The m=2.0 spectra lose some fine detail, but they are visually smoother in the small-k region and the fluctuations are largely removed. Tables V summarize the real biological results in a uniform format. For each sample we list the system and species identifier, the crop ratio c applied to the original field of view (photoreceptor rows use class-specific c so that the ensemble-averaged cropped counts \overline{N}_{crop} are comparable across receptor classes, while leaf vein rows use the original field, c=1.0), the ensemble-averaged cropped particle count \overline{N}_{crop} , and the fitted hyperuniformity exponent a0 obtained from S(k) for m=1.0 and m=2.0.

The results of real biological systems support two practical conclusions. First, modestly increasing m removes spurious small-k wiggles and improves the visual clarity of S(k) while sacrificing only limited spectral detail. Second, this smoothing does not materially change the fitted hyperuniform exponent α . The values of α obtained with m=1.0 and with m=2.0 are similar and lead to the same hyperuniform classification. In summary, the real biological tests corroborate the technical conclusions developed above. Moderate radial pooling (here m=2.0) provides a low-cost and effective remedy for fluctuations in the smallest-k bins caused by spatial truncation and finite sampling, and it does so without substantially changing the small-k decline that underlies disordered hyperuniform classification.

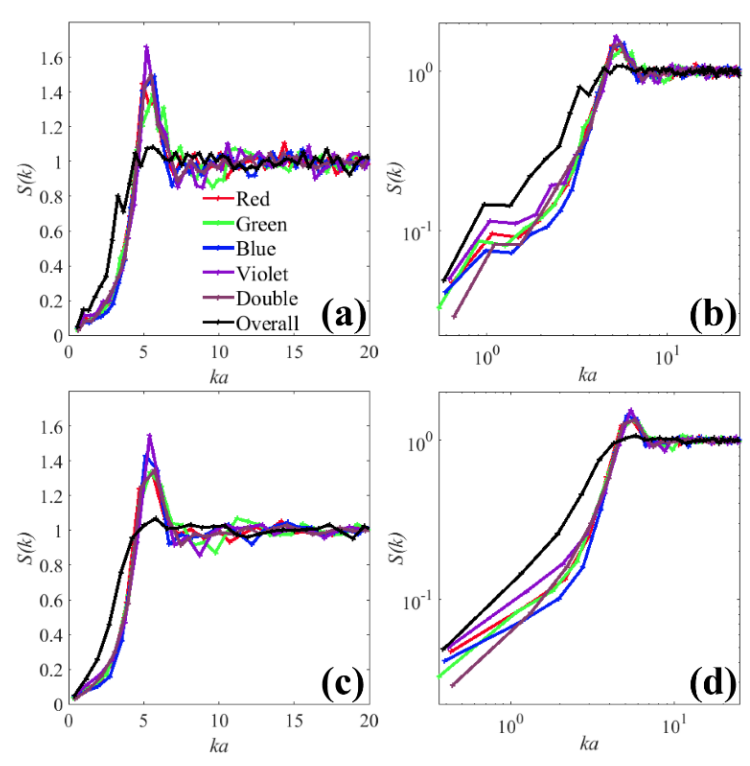


FIG.5. Structure factors for cropped avian photoreceptor patterns. Panels (a) and (b) show S(k) on a linear and a log-log scale computed with the fundamental radial bin width m=1.0. Panels (c) and (d) show the same data recomputed with m=2.0 on a linear and a log-log scale.

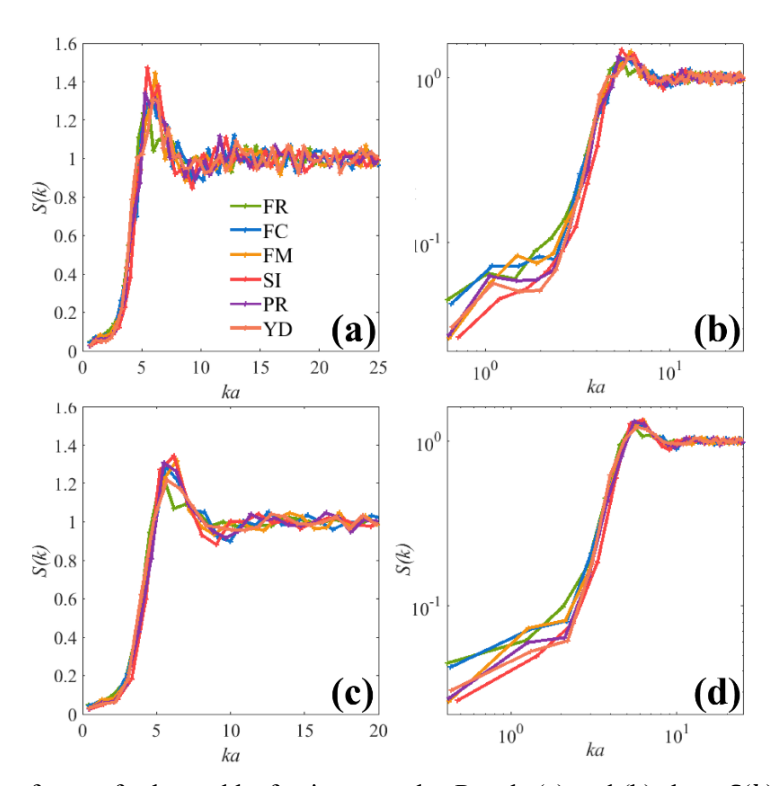


FIG.6. Structure factors for looped leaf vein networks. Panels (a) and (b) show S(k) on a linear and a log-log scale using m=1.0. Panels (c) and (d) show the same spectra computed with m=2.0 on a linear and a log-log scale.

TABLE V. Fitted hyperuniformity exponents α for real biological systems, obtained from structure factors S(k) using two radial binning parameter choices m=1.0 and m=2.0. Columns list the system and species identifier, the crop ratio c applied to the original field of view, the ensemble-averaged cropped particle count N_{crop} , and the fitted α values for m=1.0 and m=2.0. For the avian photoreceptor rows the reported crop ratios are class-specific and chosen so that N_{crop} is comparable across receptor classes; leaf vein rows report results on the original fields of view (no additional cropping, c=1.0).

system	species	С	\overline{N}_{crop}	$\alpha(m=1.0)$	$\alpha(m=2.0)$
Avian photoreceptor patterns	Red	0.5	134.0	1.35	1.30
	Green	0.5	189.2	1.21	1.21
	Blue	0.6	166.1	1.21	1.22
	Violet	0.7	143.9	1.20	1.19
	Double	0.3	128.0	1.37	1.40
	Overall	0.2	135.1	1.29	1.25
	Ficus religiosa (FR)	1.0	144.6	0.64	0.70
	Ficus caulocarpa (FC)	1.0	135.2	0.65	0.69
Leaf vein	Ficus microcarpa (FM)	1.0	142.2	0.76	0.79
networks	Smilax indica (SI)	1.0	118.4	0.78	0.77
	Populus rotundifolia (PR)	1.0	146.2	0.69	0.67
	Yulania denudate (YD)	1.0	130.0	0.63	0.61

IV. CONCLUSIONS AND DISCUSSION

We examined how finite-window sampling, implemented as random spatial truncation, and reciprocal-space radial binning affect the detection of hyperuniformity in disordered systems. Our focus was on the structure factor S(k) and the small-k hyperuniformity exponent α . The study combined controlled simulation systems of thirteen representative two-dimensional model classes with real biological examples drawn from avian photoreceptor patterns [38] and looped leaf vein networks [42]. We emphasized the experimentally relevant regime of limited ensemble size with typical ensemble averages taken over (N_c =20) independent configurations. The results below have direct implications for empirical studies of hyperuniformity.

First, random spatial truncation does not change the qualitative hyperuniform classification of a system. Systems that are non-hyperuniform in the full-field limit remain non-hyperuniform after spatial truncation. Systems that are disordered hyperuniform before truncation remain disordered hyperuniform after spatial truncation. Spatial truncation does reduce the degree of spectral suppression at the longest accessible wavelengths. Quantitatively, spatial truncation causes a significant

downward shift in the fitted spectral exponent α for large α , but the shift diminishes and becomes negligible for $\alpha \leq 1$. The corresponding real-space exponent β for the local number variance remains comparatively stable. Within the parameter ranges and sample sizes we studied, the asymptotic hyperuniformity class is preserved [3-4, 47]. Spatial truncation also preserves many short-range structural signatures, and the overall shapes of S(k) and $g_2(r)$ remain essentially unchanged.

Second, spatial truncation commonly induces configuration-dependent fluctuations in the smallest measured k bins. Two related factors drive this outcome. Spatial truncation removes true long-wavelength modes. This removal raises the relative contribution of intermediate-wavelength fluctuations to the lowest measured bins. Re-embedding after cropping also changes the effective box size L_{crop} and therefore changes the discrete reciprocal-space grid. Radial rebinning can then place bin centers at different relative positions with respect to configuration-specific spectral fine structure. These combined effects tend to accentuate small-k wiggles in the cropped data. As a result, small-k fits become more sensitive to configuration noise and to the choice of binning protocol.

Third, the spurious small-k fluctuations that appears after spatial truncation can be mitigated by moderate radial coarse-graining in reciprocal space. Increasing the radial bin width, parameterized by m, smooths configuration-dependent wiggles while preserving the broad small-k trend that determines hyperuniform classification. Care is required because overly large m removes small-k points and reduces the number of data available for fitting. Loss of those points may bias the fitted α . Based on our numerical and real biological tests, we recommend moderate radial coarse-graining with $1.0 \le m \le 3.0$. Typical stability is obtained near $m \approx 2.0$. Within this range fitted α changes little under modest adjustments of m, and the hyperuniform class inferred from scaling behavior is not changed.

In practice, we advise the following. Perform an m-scan and choose the smallest m that visibly suppresses spurious wiggles while keeping k_{min} as small as possible. Cross-check spectral inferences with the local number variance scaling. Where feasible, increase effective sampling by averaging over more configurations.

In summary, this work supports two central practical conclusions. Moderate random spatial truncation changes the fitted exponent α , but does not destroy disordered hyperuniformity order or change the hyperuniformity class. Reciprocal-space radial binning with a moderate m is an effective and low-cost remedy for sampling-induced fluctuations in the smallest-k bins, and it does not materially change the inferred hyperuniform class or substantially bias the fitted α .

Future work that would strengthen practical guidance includes systematic study of non-square and tapered windows, extension to three dimensions, and a broader treatment of anisotropic or strongly inhomogeneous empirical fields. These directions will help refine best practices for robust detection and quantification of hyperuniformity in diverse experimental contexts.

ACKNOWLEDGMENTS

This work has been supported by the National Natural Science Foundation of China (Grants No. 11274200, 12274255), the Natural Science Foundation of Shandong Province, China (Grant No. ZR2022MA055), and the foundation with Grant No. 2022NS189 from XYIAS. The authors sincerely appreciate the anonymous reviewers for devoting their precious time to reviewing our work.

REFERENCES

- [1] S. Torquato, Hyperuniform states of matter, Phys. Rep. 745, 1-95 (2018).
- [2] H. W. Haslach, Jr., Random Heterogeneous Materials: Microstructure and Macroscopic Properties, Appl. Mech. Rev. **55**, B62-B63 (2002).
- [3] S. Torquato and F. H. Stillinger, Local density fluctuations, hyperuniformity, and order metrics, Phys. Rev. E **68**, 041113 (2003).
- [4] C. E. Zachary and S. Torquato, Hyperuniformity in point patterns and two-phase random heterogeneous media, J. Stat. Mech.:Theory Exp. 2009, P12015 (2009).
- [5] G. J. Aubry, L. S. Froufe-Pérez, U. Kuhl, O. Legrand, F. Scheffold and F. Mortessagne, Experimental Tuning of Transport Regimes in Hyperuniform Disordered Photonic Materials, Phys. Rev. Lett. 125, 127402 (2020).
- [6] M. Florescu, S. Torquato and P. J. Steinhardt, Designer disordered materials with large, complete photonic band gaps, Proc. Natl. Acad. Sci. U. S. A. 106, 20658-20663 (2009).
- [7] L. S. Froufe-Pérez, M. Engel, J. J. Sáenz and F. Scheffold, Band gap formation and Anderson localization in disordered photonic materials with structural correlations, Proc. Natl. Acad. Sci. U. S. A. 114, 9570-9574 (2017).
- [8] M. A. Klatt, P. J. Steinhardt and S. Torquato, Wave propagation and band tails of two-dimensional disordered systems in the thermodynamic limit, Proc. Natl. Acad. Sci. U. S. A. 119, e2213633119 (2022).
- [9] W. Man, M. Florescu, K. Matsuyama, P. Yadak, G. Nahal, S. Hashemizad, E. Williamson, P. Steinhardt, S. Torquato and P. Chaikin, Photonic band gap in isotropic hyperuniform disordered solids with low dielectric contrast, Opt. Express 21, 19972-19981 (2013).
- [10] O. Christogeorgos, H. Zhang, Q. Cheng and Y. Hao, Extraordinary Directive Emission and Scanning from an Array of Radiation Sources with Hyperuniform Disorder, Phys. Rev. Appl. 15, 014062 (2021).
- [11] R. D. Batten, F. H. Stillinger and S. Torquato, Novel Low-Temperature Behavior in Classical Many-Particle Systems, Phys. Rev. Lett. **103**, 050602 (2009).
- [12] R. D. Batten, F. H. Stillinger and S. Torquato, Interactions leading to disordered ground states and unusual low-temperature behavior, Phys. Rev. E **80**, 031105 (2009).
- [13] Q. Le Thien, D. Mcdermott, C. J. O. Reichhardt and C. Reichhardt, Enhanced pinning for vortices in hyperuniform pinning arrays and emergent hyperuniform vortex configurations with quenched disorder, Phys. Rev. B **96**, 094516 (2017).
- [14] D. Chen and S. Torquato, Designing disordered hyperuniform two-phase materials with novel physical properties, Acta Mater. **142**, 152-161 (2018).
- [15] M. Skolnick and S. Torquato, Simulated diffusion spreadability for characterizing the structure and transport properties of two-phase materials, Acta Mater. 250, 118857 (2023).
- [16] S. Torquato, Diffusion spreadability as a probe of the microstructure of complex media across length scales, Phys. Rev. E **104**, 054102 (2021).
- [17] H. Wang and S. Torquato, Dynamic Measure of Hyperuniformity and Nonhyperuniformity in Heterogeneous Media via the Diffusion Spreadability, Phys. Rev. Appl. 17, 034022 (2022).
- [18] E. Nocerino, Emergent properties and the multiscale characterization challenge in condensed matter, from crystals to complex materials: a review, J. Phys. D: Appl. Phys. **58**, 393001 (2025).
- [19] J. S. Brauchart, P. J. Grabner and W. Kusner, Hyperuniform Point Sets on the Sphere: Deterministic

- Aspects, Constr. Approx. 50, 45-61 (2019).
- [20] J. S. Brauchart, P. J. Grabner, W. Kusner and J. Ziefle, Hyperuniform point sets on the sphere: probabilistic aspects, Monatsh. Math. 192, 763-781 (2020).
- [21] S. Ghosh and J. L. Lebowitz, Generalized Stealthy Hyperuniform Processes: Maximal Rigidity and the Bounded Holes Conjecture, Commun. Math. Phys. **363**, 97-110 (2018).
- [22] S. Torquato, G. Zhang and M. De Courcy-Ireland, Hidden multiscale order in the primes, J. Phys. A:Math. Theor. **52**, 135002 (2019).
- [23] E. Newby, W. Shi, Y. Jiao, R. Albert and S. Torquato, Structural properties of hyperuniform Voronoi networks, Phys. Rev. E 111, 034123 (2025).
- [24] Z.-Q. Li, Q.-L. Lei and Y.-Q. Ma, Fluidization and anomalous density fluctuations in 2D Voronoi cell tissues with pulsating activity, Proc. Natl. Acad. Sci. U. S. A. 122, e2421518122 (2025).
- [25] D. Chen, R. Samajdar, Y. Jiao and S. Torquato, Anomalous suppression of large-scale density fluctuations in classical and quantum spin liquids, Proc. Natl. Acad. Sci. U. S. A. 122, e2416111122 (2025).
- [26] J. Wang, Z. Sun, H. Chen, G. Wang, D. Chen, G. Chen, J. Shuai, M. Yang, Y. Jiao and L. Liu, Hyperuniform Networks of Active Magnetic Robotic Spinners, Phys. Rev. Lett. 134, 248301 (2025).
- [27] R. J. H. Ross, G. D. Masucci, C. Y. Lin, T. L. Iglesias, S. Reiter and S. Pigolotti, Hyperdisordered Cell Packing on a Growing Surface, Phys. Rev. X 15, 021064 (2025).
- [28] L. Y. Zhong and S. Mao, Construction of digital realizations of anisotropic hyperuniform continuous random fields in two and three dimensions via generalized spectral filtering, Phys. Rev. E 112, 044136 (2025).
- [29] C. E. Maher and S. Torquato, Hyperuniformity scaling of maximally random jammed packings of two-dimensional binary disks, Phys. Rev. E **110**, 064605 (2024).
- [30] N. Wang, Y. Tong, F. Liu, X. Li, Y. He and W. Fan, Turing instability-induced oscillations in coupled reaction-diffusion systems, Chin. Phys. B **34**, 038201 (2025).
- [31] N. Liang, Y. Wang and B. Song, Disordered hyperuniformity and thermal transport in monolayer amorphous carbon, SCI CHINA PHYS MECH **68**, 226111 (2025).
- [32] Y. Liu and M. Chen, Multihyperuniformity in high-entropy MXenes, Appl. Phys. Lett. **126**, 013101 (2025).
- [33] C. E. Maher and K. A. Newhall, Characterizing the hyperuniformity of disordered network metamaterials, Phys. Rev. E 111, 065420 (2025).
- [34] S. Mitra, I. Mukherjee and P. K. Mohanty, Percolation of systems having hyperuniformity or giant number fluctuations, Phys. Rev. E 112, 014120 (2025).
- [35] W. Shi, Y. Jiao and S. Torquato, Three-dimensional construction of hyperuniform, nonhyperuniform, and antihyperuniform disordered heterogeneous materials and their transport properties via spectral density functions, Phys. Rev. E 111, 035310 (2025).
- [36] L. Zhong, S. Mao and Y. Jiao, Modeling disordered hyperuniform heterogeneous materials: Microstructure representation, field fluctuations and effective properties, Acta Mater. 296, 121218 (2025).
- [37] Y. F. Si, D. Wang, Y. Z. Jiang, H. Zhu, S. Shi, L. Tan and L. M. Yang, Bionic Intelligent Clothing, Adv. Mater., e14621 (2025).
- [38] Y. Jiao, T. Lau, H. Hatzikirou, M. Meyer-Hermann, C. C. Joseph and S. Torquato, Avian photoreceptor patterns represent a disordered hyperuniform solution to a multiscale packing

- problem, Phys. Rev. E 89, 022721 (2014).
- [39] A. Mayer, V. Balasubramanian, T. Mora and A. M. Walczak, How a well-adapted immune system is organized, Proc. Natl. Acad. Sci. U. S. A. 112, 5950-5955 (2015).
- [40] Z. Ge, The hidden order of Turing patterns in arid and semi-arid vegetation ecosystems, Proc. Natl. Acad. Sci. U. S. A. 120, e2306514120 (2023).
- [41] W. S. Hua, L. J. Cui, M. Delgado-Baquerizo, R. Solé, S. Kéfi, M. Berdugo, N. Xu, B. Wang, Q. X. Liu and C. Xu, Causes and consequences of disordered hyperuniformity in global drylands, Proc. Natl. Acad. Sci. U. S. A. 122, e2504496122 (2025).
- [42] Y. Liu, D. Chen, J. Tian, W. Xu and Y. Jiao, Universal Hyperuniform Organization in Looped Leaf Vein Networks, Phys. Rev. Lett. **133**, 028401 (2024).
- [43] L. Berthier, P. Chaudhuri, C. Coulais, O. Dauchot and P. Sollich, Suppressed Compressibility at Large Scale in Jammed Packings of Size-Disperse Spheres, Phys. Rev. Lett. **106**, 120601 (2011).
- [44] C. E. Zachary, Y. Jiao and S. Torquato, Hyperuniform Long-Range Correlations are a Signature of Disordered Jammed Hard-Particle Packings, Phys. Rev. Lett. 106, 178001 (2011).
- [45] C. E. Zachary, Y. Jiao and S. Torquato, Hyperuniformity, quasi-long-range correlations, and void-space constraints in maximally random jammed particle packings. I. Polydisperse spheres, Phys. Rev. E **83**, 051308 (2011).
- [46] C. E. Zachary, Y. Jiao and S. Torquato, Hyperuniformity, quasi-long-range correlations, and void-space constraints in maximally random jammed particle packings. II. Anisotropy in particle shape, Phys. Rev. E 83, 051309 (2011).
- [47] C. E. Zachary and S. Torquato, Anomalous local coordination, density fluctuations, and void statistics in disordered hyperuniform many-particle ground states, Phys. Rev. E 83, 051133 (2011).
- [48] S. Torquato, Disordered hyperuniform heterogeneous materials, J. Phys.:Condens. Matter 28, 414012 (2016).
- [49] S. Torquato, G. Zhang and F. H. Stillinger, Ensemble Theory for Stealthy Hyperuniform Disordered Ground States, Phys. Rev. X 5, 021020 (2015).
- [50] G. Zhang, F. H. Stillinger and S. Torquato, Transport, geometrical, and topological properties of stealthy disordered hyperuniform two-phase systems, J. Chem. Phys. **145**, 244109 (2016).
- [51] H. Wang and S. Torquato, Designer pair statistics of disordered many-particle systems with novel properties, J. Chem. Phys. **160**, 044911 (2024).
- [52] G. Zhang and S. Torquato, Realizable hyperuniform and nonhyperuniform particle configurations with targeted spectral functions via effective pair interactions, Phys. Rev. E **101**, 032124 (2020).
- [53] J. W. Evans, Random and cooperative sequential adsorption, Rev. Mod. Phys. 65, 1281-1329 (1993).
- [54] J. Feder, Random sequential adsorption, J. Theor. Biol. 87, 237-254 (1980).
- [55] A. F. Karr, D. J. Daley and D. Vere-Jones, An Introduction to the Theory of Point Processes, J. Am. Stat. Assoc. **85**, 262 (1990).
- [56] Q. Chen and J. Tian, A connection between the density and temperature of the Lennard-Jones fluids at equilibrium and the first peak of the radial distribution function, Fluid Phase Equilib. **567**, 113709 (2023).
- [57] J. E. Jones, On the determination of molecular fields. II. From the equation of state of gas, Proc. Roy. Soc. A 106, 463-477 (1924).
- [58] L. Verlet, Computer "Experiments" on Classical Fluids. I. Thermodynamical Properties of Lennard-Jones Molecules, Phys. Rev. 159, 98-103 (1967).

- [59] X. Li and J. Tian, Determining state points through the radial distribution function of Yukawa fluids at equilibrium, Fluid Phase Equilib. **589**, 114270 (2025).
- [60] H. Yukawa, On the Interaction of Elementary Particles. I, Prog. Theor. Phys. Suppl. 1, 1-10 (1955).
- [61] L. E. Silbert and M. Silbert, Long-wavelength structural anomalies in jammed systems, Phys. Rev. E 80, 041304 (2009).
- [62] O. U. Uche, F. H. Stillinger and S. Torquato, Constraints on collective density variables: Two dimensions, Phys. Rev. E **70**, 046122 (2004).